

Analysis of Graphene-Based Photonic Crystal Fiber Sensor Using Birefringence and Surface Plasmon Resonance

Xianchao Yang¹ · Ying Lu¹ · Baolin Liu¹ · Jianquan Yao¹

Received: 7 March 2016 / Accepted: 31 May 2016 / Published online: 20 June 2016
© Springer Science+Business Media New York 2016

Abstract We present and numerically characterize a photonic crystal fiber (PCF)-based surface plasmon resonance (SPR) sensor. By adjusting the air hole sizes of the PCF, the effective refractive index (RI) of core-guided mode can be tuned effectively and the sensor exhibits strong birefringence. Alternate holes coated with graphene-Ag bimetallic layers in the second layer are used as analyte channels, which can avoid adjacent interference and improve the signal to noise ratio (SNR). The graphene's good features can not only solve the problem of silver oxidation but also increase the absorption of molecules. We theoretically analyze the influence of the air hole sizes of the PCF and the thicknesses of graphene layer and Ag layer on the performance of the designed sensor using wavelength and amplitude interrogations. The wavelength sensitivity we obtained is as high as 2520 nm/RIU with the resolution of 3.97×10^{-5} RIU, which can provide a reference for developing a high-sensitivity, real-time, fast-response, and distributed SPR sensor.

Keywords Photonic crystal fiber · Surface plasmon resonance · Graphene-Ag bimetallic layers · Birefringence · Wavelength and amplitude interrogations

Introduction

Surface plasmon resonance (SPR) technique has brought tremendous advancements in different fields due to its label-free and highly sensitive detection properties. In the SPR technique, a transverse magnetic (TM) or p-polarized light causes the excitation of electron density oscillations (known as surface plasmon wave, SPW) at the metal-dielectric interface. When the energy and the momentum of the incident light and SPW match, a resonance occurs [1]. The necessary condition for SPR is

$$\frac{2\pi}{\lambda} \sqrt{\varepsilon_p} \sin\theta = \frac{2\pi}{\lambda} \left(\frac{\varepsilon_m \varepsilon_s}{\varepsilon_m + \varepsilon_s} \right)^{1/2} \quad (1)$$

where λ is the light wavelength, θ is the angle of incident light, ε_p represents the dielectric constant of the material on which metal is deposited, and ε_m and ε_s are the dielectric constants of the metal and the sensing medium, respectively. When SPR occurs, the energy will be transferred from the incident light to surface plasmons (SPs), which reduce the intensity of the reflected light significantly and result in a sharp dip at the particular wavelength. The resonance parameters (λ and θ) depend on the refractive index (RI) of sensing medium strongly. Then we can detect analyte RI by monitoring the resonance peak. Since the first sensing application of SPR technique was reported in 1983 [2], numerous kinds of SPR sensors for physical, chemical, and biochemical sensing have been reported. The earliest SPR sensing devices are prism based [1, 3–5], which can realize extremely high resolution of 10^{-6} RIU. But its bulky size and mechanical instability make it impossible for remote sensing and highly integrate.

Optical fiber-based SPR sensors [6, 7] overcome these shortcomings as the sensing probe can be miniaturized. Usually, the fiber is tapered or side polished and then coated

✉ Ying Lu
luying@tju.edu.cn

¹ College of Precision Instrument and Opto-Electronics Engineering, Key Laboratory of Opto-Electronics Information Technology (Ministry of Education), Tianjin University, Tianjin 300072, People's Republic of China

with a metal layer to form a sensing region. Gold and silver are the most widely used SPR metals in sensing applications. Gold is chemically stable and shows a larger shift of resonance wavelength, but it has certain limitations like larger absorption coefficient leading to a broader resonance peak, formation of island in very thin layers, band to band transition, and surface roughness arising due to thermal evaporation [8]. Silver shows a sharper resonance peak compared to gold which can increase the detection accuracy. However, it gets oxidized easily when used in liquid or gaseous environments. To solve the oxidization problem, some researchers proposed Au–Ag bimetallic structure SPR sensors [9, 10]. Ag is the major SPR metal used to support SPs, and Au is the outer-protective layer used to improve the sensor's chemical stability. Recently, graphene has been used as a coating on the metal surface for SPR-based sensors due to its various advantages [11]. Graphene's high electron density of hexagonal rings does not allow atoms as small as helium to pass through it, which can prevent oxidation of metal surface. Other features such as high surface to volume ratio, broadband optical, and plasmonic properties make it an appropriate candidate to be used as a functional coating material for existing plasmonic devices [12, 13]. Moreover, graphene-based SPR sensors show higher adsorption of molecules due to π – π stacking, which can be effectively used for biochemical sensing.

The appearance of photonic crystal fibers (PCFs) is a breakthrough in fiber-optic technology, leading to unprecedented properties that overcome many limitations [14]. The flexible design and unique structure make it own many advantages like single-mode propagation, high confinement, controllable birefringence, and so on. Moreover, the effective index of the core-guided mode can be tailored by changing the geometrical parameters of the structure, which helps in phase matching of core-guided mode and plasmon mode. PCF can potentially be made highly birefringent as the fabrication process permits the formation of the required microstructure near the fiber core [15], which can be widely used in fiber loop mirrors [16] or polarization filters [17, 18]. PCF-based sensor also has a better mechanical stability than ordinary fiber based as it need not strip the fiber jacket and cladding, which destroy the fiber integrity. Taking the advantages of SPR, graphene coating, and PCF, the same type sensors have been very recently reported. In [19], Dash et al. proposed a graphene–Ag-based D-shaped PCF biosensor using SPR and the wavelength sensitivity is 3700 nm/RIU with a resolution of 2.7×10^{-5} RIU. The PCF is side polished to form a D-shaped structure, which is quite difficult to operate. In [6], Hongyan Fu et al. presented a graphene–Au-based fiber-optic SPR biosensor. The cladding of a single-mode fiber is stripped to form a ring structure, and the graphene–Au bimetallic layers are deposited on the fiber core. The influence of the thicknesses of Au film and graphene layer on the sensor is analyzed. But the resonance wavelength and the effective

index of the core-guided mode cannot be easily tuned as the RI of the single-mode fiber core is fixed.

In this paper, we present a PCF-based SPR sensor coated with graphene–Ag bimetallic layers. The asymmetrical structure leads to strong birefringence with x -polarized peak providing much higher peak loss and sensitivity than the y -polarized. The central air hole is used to tune the effective RI (n_{eff}) of the core-guided mode, which can affect the mode coupling efficiently. We theoretically analyze the influence of the air hole sizes of the PCF and the thicknesses of the graphene layer and Ag layer on the performance of the designed sensor using wavelength and amplitude interrogations. The wavelength sensitivity obtained is as high as 2520 nm/RIU with the resolution of 3.97×10^{-5} RIU by optimizing the parameters.

Structure and Theoretical Modeling

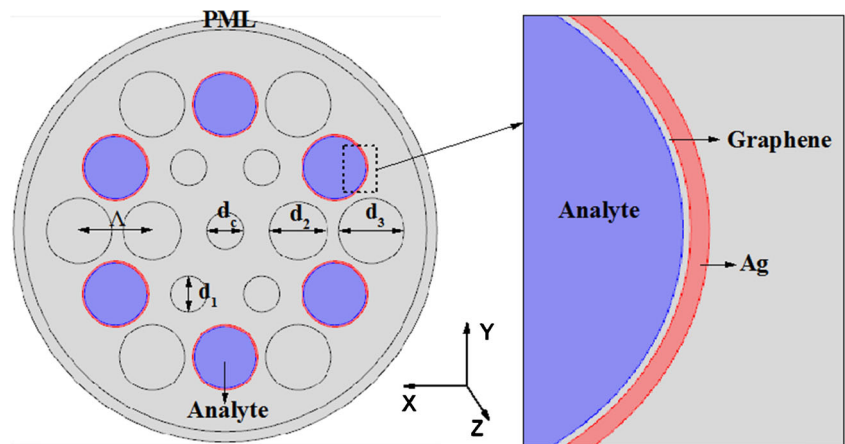
As shown in Fig. 1, the cladding of the sensor consists of two layers of air holes arranged in a hexagonal manner and the core is a central air hole. The structure can be fabricated using the standard stack-and-draw method. The central hole is used to lower the RI of core-guided mode to facilitate the phase matching with the plasmon mode. The asymmetrical structure caused by the two larger holes in the first layer leads to strong birefringence, which helps in coupling more light into a particular direction, resulting in x -polarized resonance peak more sensitive and much stronger than the y -polarized. The larger holes in the second layer are selectively coated with graphene–Ag bimetallic layers as it demonstrates better signal to noise ratio (SNR) compared with the entirely coated structure [20, 21]. Moreover, graphene–Ag bimetallic layer-coated sensor shows a sharper resonance peak compared to graphene–Au bimetallic layers [11, 22] and is more sensitive compared to Au–Ag bimetallic layers [23]. Coating of the metal layer can be performed with a chemical vapor deposition technique [24] or a wet chemistry deposition technique [25]. A single or few layers of graphene can be isolated and deposited on a silver surface using several available techniques [26, 27]. Selective coating and analyte filling are possible as described in [28] and [29], respectively.

In Fig. 1, the optimized structural parameters are $\Lambda = 2 \mu\text{m}$, $d_1/\Lambda = 0.5$, $d_2/\Lambda = 0.5$, $d_3/\Lambda = 0.8$, $d_4/\Lambda = 0.9$, and $t_{\text{Ag}} = 50 \text{ nm}$, where t_{Ag} is the thickness of the Ag layer. The fiber material is fused silica and the RI is determined by Sellmeier equation [30]:

$$n^2(\lambda) = 1 + \frac{A_1 \lambda^2}{\lambda^2 - B_1} + \frac{A_2 \lambda^2}{\lambda^2 - B_2} + \frac{A_3 \lambda^2}{\lambda^2 - B_3} \quad (2)$$

where $A_1 = 0.696166300$, $A_2 = 0.407942600$, $A_3 = 0.897479400$, $B_1 = 4.67914826 \times 10^{-3} \mu\text{m}^2$, $B_2 = 1.35120631 \times 10^{-2} \mu\text{m}^2$, and

Fig. 1 Schematic of the designed sensor



$B_3 = 97.9340025 \mu\text{m}^2$. The RI of graphene can be obtained by the following equation [19]:

$$n_g = 3 + \frac{iC_1\lambda}{3} \tag{3}$$

where $C_1 = 5.446 \mu\text{m}^{-1}$ and λ is the vacuum wavelength. Each single layer of graphene has a thickness of 0.34 nm. The total thickness of the graphene layer is $0.34 \times L$ where L is the number of graphene layers. In Fig. 1, $L = 9$. The RI of Ag is given by the Handbook of Optics [31].

Finite element method (FEM) is used for calculation using COMSOL Multiphysics software. We use perfectly matched layers (PML) as the boundary condition, and the whole section of the sensor is divided into many triangular subdomains. The total number of mesh elements is 183,578. As shown in Fig. 1, the simulation for modal analysis is done in the XY plane while the light propagation is along the Z direction.

Results and Discussion

Figure 2a shows the 2-D and 3-D electric field distributions of the sensor at the resonance wavelength $\lambda = 590 \text{ nm}$. We can see that the sensor exhibits strong birefringence due to the asymmetrical structure, and the light mainly propagates along the y direction. When SPR occurs, some of the energy will be transferred from the core to the metal-dielectric interface and the intensity of the reflected light will be reduced. To make a better understanding, we plot the electric field intensity distribution at the middle of the sensor along y-axis with SPR layers and without SPR layers in Fig. 2b. As we have seen, the core-guided modes are confined well into the fiber core and only a part of energy is transferred to the metal-dielectric interface. Moreover, both sides of the metal layer can excite SPs, but the resonance intensity at the metal-sensing medium interface is much stronger than that at the metal-dielectric interface. The amplitude of electric field has a maximum value at the metal

surface and decays exponentially away from it, which is in good agreement with the excitation of SPs.

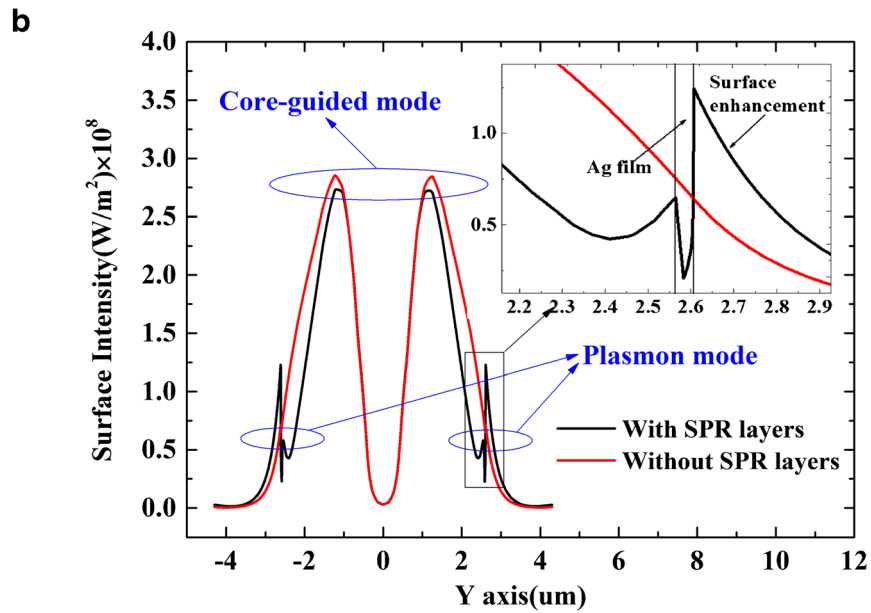
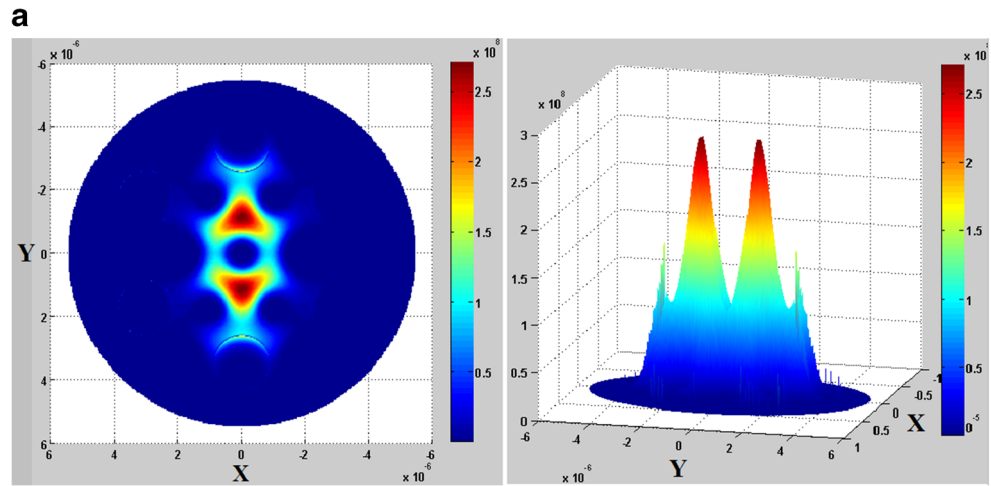
Figure 3 shows the dispersion relations and electric field distributions of the core-guided modes and the plasmon mode when analyte RI $n_a = 1.33$. We use the Gaussian-like modes as the core-guided modes which are best suited for the excitation by standard Gaussian laser sources [32]. As shown in Fig. 3, the core modes exhibit strong birefringence with two n_{eff} curves (black solid curve and black dotted curve) of the core-guided modes, resulting in two intersections (dots (d) and (e)) with the plasmon mode (red solid curve) and two resonance peaks (blue solid curve and blue dotted curve) for the same analyte RI. Resonance occurs at the point where the real part of n_{eff} ($\text{Re}(n_{\text{eff}})$) of the core-guided mode and plasmon mode matches. We define one component of the core-guided modes being polarized essentially parallel to the y-axis as y-polarized mode and the other orthogonal to it as x-polarized mode. As we have seen, x-polarized mode is much stronger than the y-polarized.

Figure 4a shows x-polarized and y-polarized peaks when n_a varies from 1.33 to 1.34. From the picture, we can see that x-polarized and y-polarized peaks all redshift when n_a increases because the increase of n_a changes $\text{Re}(n_{\text{eff}})$ of the plasmon mode, which in turn changes the phase matching point between the core-guided mode and the plasmon mode. When n_a is approaching fiber core n_{eff} , the peak losses all increase as the mode coupling is enhanced. But the x-polarized peak has a much sharper resonance peak and higher peak loss than the y-polarized. For example, when $n_a = 1.33$, the confinement loss of the x-polarized peak is $1.887 \times 10^2 \text{ dB/cm}$, about 10 times higher than the y-polarized peak of $1.88 \times 10 \text{ dB/cm}$. The confinement loss is defined as follows [32]:

$$\alpha_{\text{loss}} \left(\frac{\text{dB}}{\text{m}} \right) = 8.686 \cdot k_0 \text{Im}[n_{\text{eff}}] \tag{4}$$

where $k_0 = 2\pi/\lambda$ is the wavenumber with λ in meters and $\text{Im}(n_{\text{eff}})$ is the imaginary part of mode n_{eff} . A sharper resonance peak improves the detection accuracy in terms of

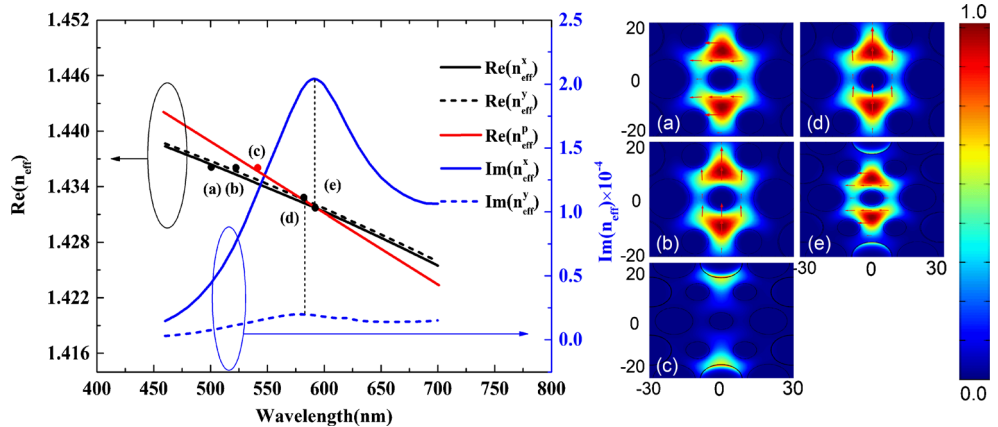
Fig. 2 **a** 2-D and 3-D electric field distributions of the fundamental mode at resonance wavelength $\lambda = 590$ nm. **b** Electric field intensity distribution at the middle of the sensor along the y -axis at resonance wavelength $\lambda = 590$ nm



SNR. Moreover, the x -polarized peak generates a larger shift (23 nm) than the y -polarized (21 nm). In wavelength interrogation, the wavelength sensitivity is defined as [32]

$$S_{\lambda}(\text{nm}/\text{RIU}) = \frac{\Delta\lambda_{\text{peak}}}{\Delta n_a} \tag{5}$$

Fig. 3 (Left) Dispersion relations and electric field distributions of core-guided modes and the plasmon mode with $n_a = 1.33$. (Right) Insets—**a** x -polarized core mode at $\lambda = 500$ nm; **b** y -polarized core mode at $\lambda = 500$ nm; **c** plasmon mode at $\lambda = 617$ nm; **d** y -polarized core mode at $\lambda = 579$ nm (phase matching point); **e** x -polarized core mode at $\lambda = 590$ nm (phase matching point)



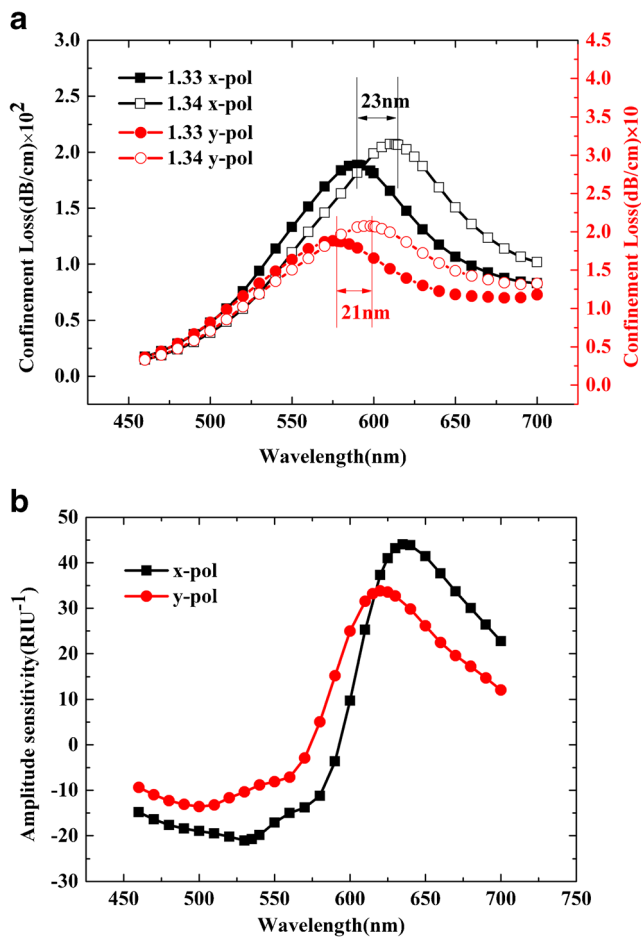


Fig. 4 **a** Loss spectra of *x*- and *y*-polarized peaks with $n_a = 1.33$ and 1.34 . **b** Amplitude sensitivities of *x*- and *y*-polarized peaks with n_a changes from 1.33 to 1.34

where $\Delta\lambda_{\text{peak}}$ is the wavelength shift and Δn_a is the variation of analyte RI. Then *x*-polarized resonance peak has a higher wavelength sensitivity (2300 nm/RIU) than the *y*-polarized (2100 nm/RIU).

In amplitude interrogation, the measurement is done at a single wavelength and does not require spectral manipulation. The operation is simple and low cost but has a lower sensitivity. Assume that the light wavelength is λ , the transmission length is L , and the loss of core mode as a function of wavelength is $\alpha(\lambda, n_a)$. The amplitude sensitivity can be defined as [32]

$$S(\text{RIU}^{-1}) = -(\partial\alpha(\lambda, n_a)/\partial n_a)/\alpha(\lambda, n_a) \quad (6)$$

Figure 4b shows the amplitude sensitivities of *x*-polarized and *y*-polarized peaks when n_a changes from 1.33 to 1.34 . The *x*-polarized peak has a higher amplitude sensitivity (44 RIU^{-1}) than the *y*-polarized (33.8 RIU^{-1}) as it has a stronger mode coupling.

In conclusion, the *x*-polarized peak is more suitable for RI sensing as it has better SNR, larger confinement loss, higher

wavelength, and amplitude sensitivities. So we only consider the *x*-polarized peak in the next section.

We calculate an analyte RI range from 1.33 to 1.35 with the steps of 0.005 to investigate the sensor’s performance. As shown in Fig. 5, the resonance peak shifts to the longer wavelength and the peak loss increases with n_a increasing. According to Eq. (5), the wavelength sensitivities are 1800 , 2000 , 2600 , and 3400 nm/RIU , respectively. The sensor shows a higher wavelength sensitivity for the high analyte RI change than the low. This is because when n_a approaches the n_{eff} of the core-guided mode (about 1.45), the coupling between the core-guided mode and plasmon mode will be enhanced, leading to a higher wavelength sensitivity and larger peak loss.

The n_{eff} of the core-guided mode can be tuned effectively by adjusting the central air hole size, which has a great influence on the sensor’s performance. As shown in Fig. 6a, when d_c increases, the resonance wavelength redshifts slowly but the resonance intensity increases largely. With d_c is increasing, as shown in Fig. 6b, the resonance wavelength redshifts and the resonance intensity increases continuously. But the peak wavelength shift $\Delta\lambda_{\text{peak}}$ goes through a circle of rise and fall. When $d_c/\Lambda = 0.5$, it reaches the maximum value of 24 nm . Whether the central hole gets larger or smaller, $\Delta\lambda_{\text{peak}}$ all decrease. According to Eq. (5), the wavelength sensitivity will change in the same way. This is because a larger central hole will lower the n_{eff} of the core-guided mode, making it close to the analyte RI. Besides, the more expulsion of field from fiber core leads to the increment in modal field at the metal-dielectric interface then the mode coupling will be enhanced. But when the central hole is too big, incident light will not be confined well in the core then the mode coupling will weaken. As to amplitude sensitivity, it increases slightly which can be neglected. When $d_c/\Lambda = 0.3, 0.4,$ and 0.5 , the amplitude sensitivities are $42, 42.9,$ and 44 RIU^{-1} , respectively.

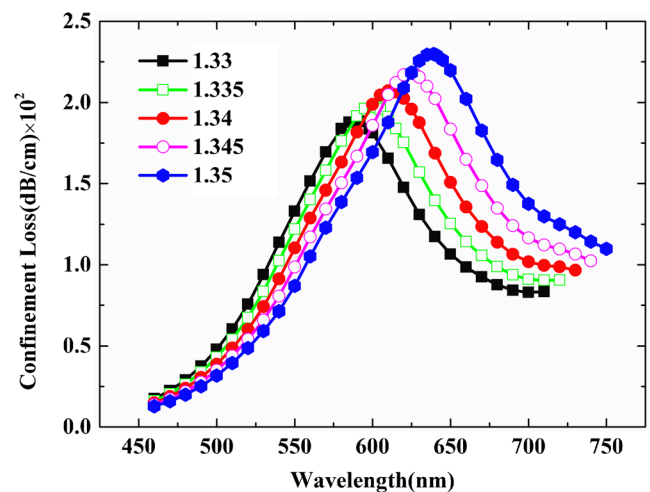


Fig. 5 Loss spectra of the designed sensor when n_a varies from 1.33 to 1.35 with the steps of 0.005

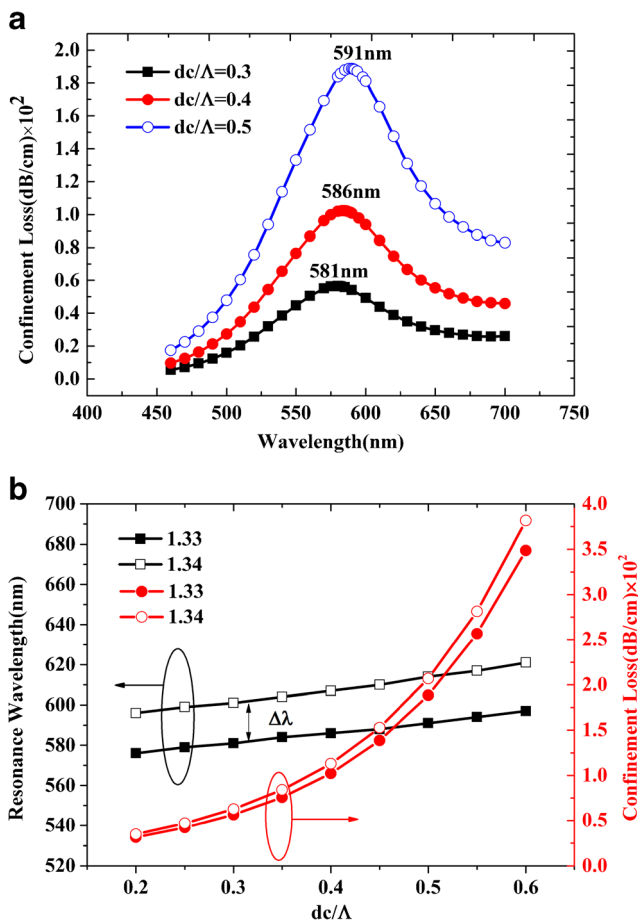


Fig. 6 **a** Loss spectra of the designed sensor when $d_c/\Lambda = 0.3, 0.4,$ and 0.5 with $n_a = 1.33$. **b** Peak loss and peak wavelength of the designed sensor for various values of d_c with $n_a = 1.33$ and 1.34

The asymmetrical structure of the sensor is mainly caused by two larger holes in the first layer, which can affect the birefringence of the sensor significantly. As shown in Fig. 7a, when d_2/Λ increases from 0.6 to 0.8, the resonance peak redshifts from 586 to 588 nm and the peak loss increases from 1.032×10^2 to 1.887×10^2 dB/cm, which means that d_2 mainly affects the resonance intensity of the sensor. Figure 7b shows the amplitude sensitivities when $d_2/\Lambda = 0.6, 0.7,$ and 0.8 . We can see that the amplitude sensitivities are nearly unchanged. As a result, the birefringence intensity can be tailored by adjusting d_2 , which can be used in fiber loop mirrors or polarization filters as described in [16–18].

SPW is very sensitive to the thickness of the metal layer and then different thicknesses of the Ag layers from 20 to 50 nm with the steps of 10 nm are analyzed. The loss spectra of the sensor with different silver layers are shown in Fig. 8a. We can see that the resonance peak damps obviously with t_{Ag} increasing, which means that a thicker Ag layer leads to a worse SNR. Also the amplitude sensitivity decreases from 72.47 to 32.57 RIU^{-1} as shown in Fig. 8b. But in Fig. 8c, the average wavelength sensitivity increases from 1900 to

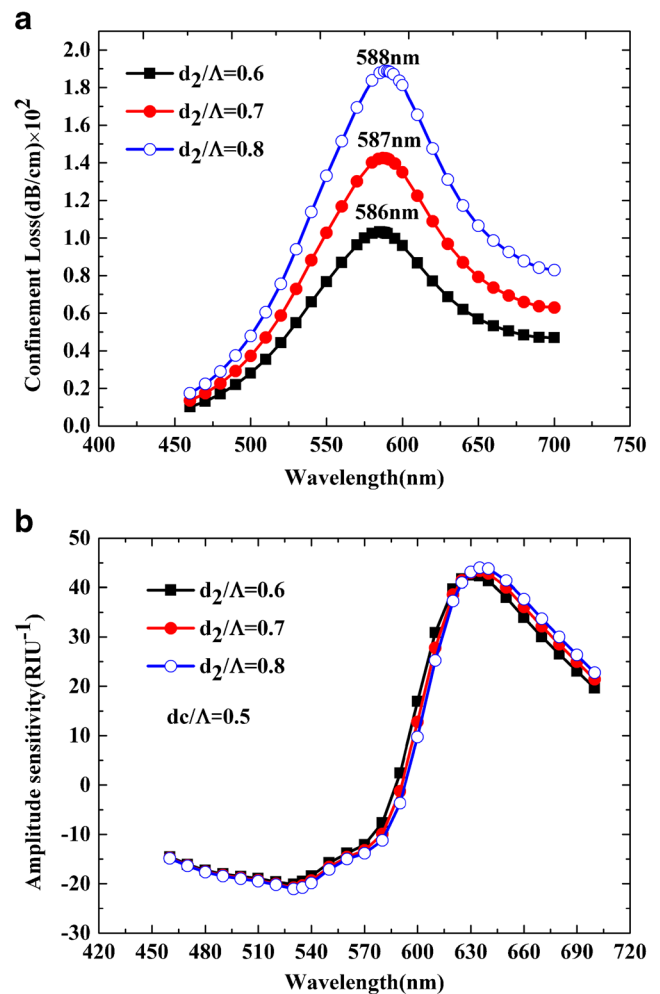


Fig. 7 **a** Loss spectra of the designed sensor when $d_2/\Lambda = 0.3, 0.4, 0.5$ with $n_a = 1.33$ and $d_c/\Lambda = 0.5$. **b** Amplitude sensitivities of the designed sensor when $d_2/\Lambda = 0.3, 0.4, 0.5$ with $n_a = 1.33$ and $d_c/\Lambda = 0.5$

2520 nm/RIU with t_{Ag} increases from 20 to 50 nm. Therefore, there is a trade among confinement loss, wavelength, and amplitude sensitivities which can be optimized as the specific requirement. If the spectrograph resolution is 0.1 nm, the highest resolution of the sensor is 3.97×10^{-5} , which is comparable to the same type sensors [19].

Figure 9a shows the loss spectra of the sensor with increase in the number of graphene layers. The resonance intensity decreases from 1.89×10^2 to 1.73×10^2 dB/cm, and the resonance wavelength shifts from 590 to 630 nm with L increases from 9 to 15. Moreover, the amplitude sensitivity will also decrease as shown in Fig. 9b because the graphene layer will screen the core-guided mode from the plasmon mode. The increase in graphene thickness leads to the increase in the n_{eff} at the metal-dielectric interface which results in the resonance condition satisfied at a longer wavelength as shown in Fig. 3. The peak loss damp is caused by the imaginary part of the dielectric constant of the graphene layer. Therefore, a thinner graphene layer can get a sharper resonance peak and a higher

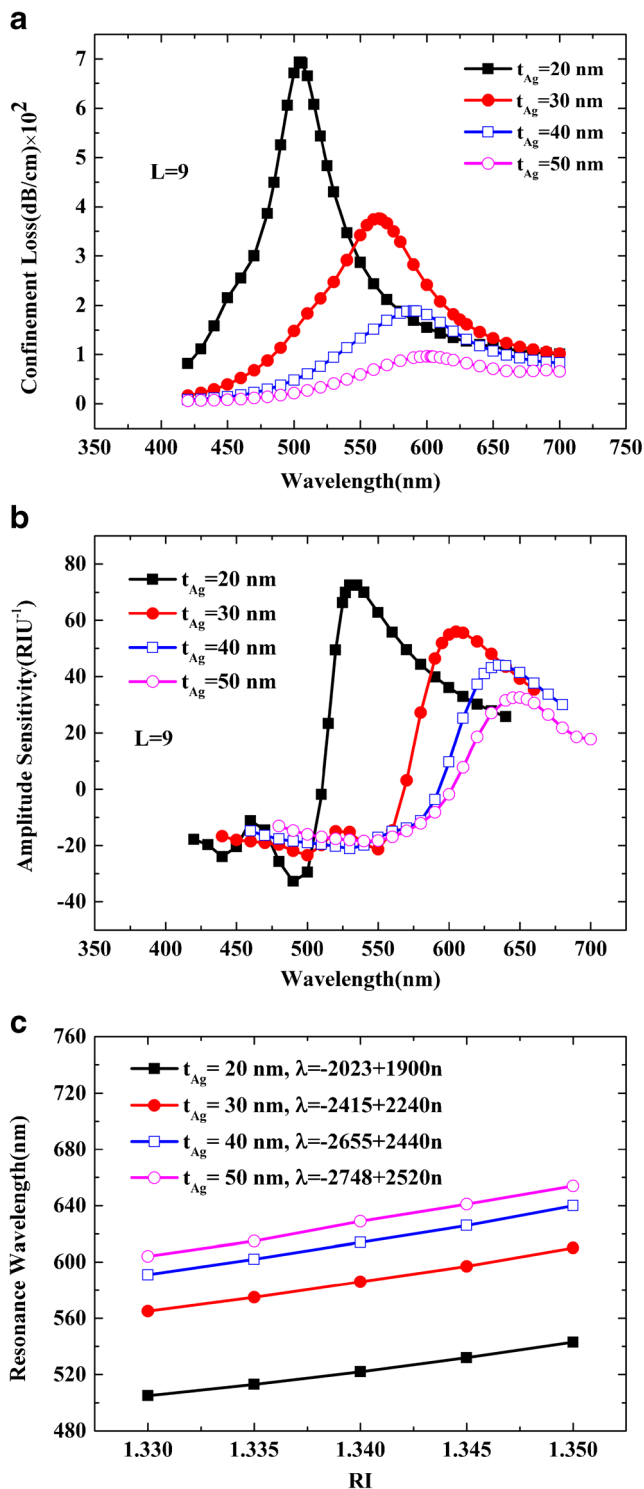


Fig. 8 **a** Loss spectra of the designed sensor for various values of t_{Ag} with $n_a = 1.33$, $d_c/\Lambda = 0.5$, and $d_2/\Lambda = 0.8$. **b** Peak wavelength of the designed sensor for various values of t_{Ag} when n_a varies from 1.33 to 1.35 with $d_c/\Lambda = 0.5$ and $d_2/\Lambda = 0.8$. **c** Amplitude sensitivities of the designed sensor for various values of t_{Ag} with $n_a = 1.33$, $d_c/\Lambda = 0.5$, and $d_2/\Lambda = 0.8$

sensitivity. In practice, to get a better performance, the graphene layer should be as thin as possible.

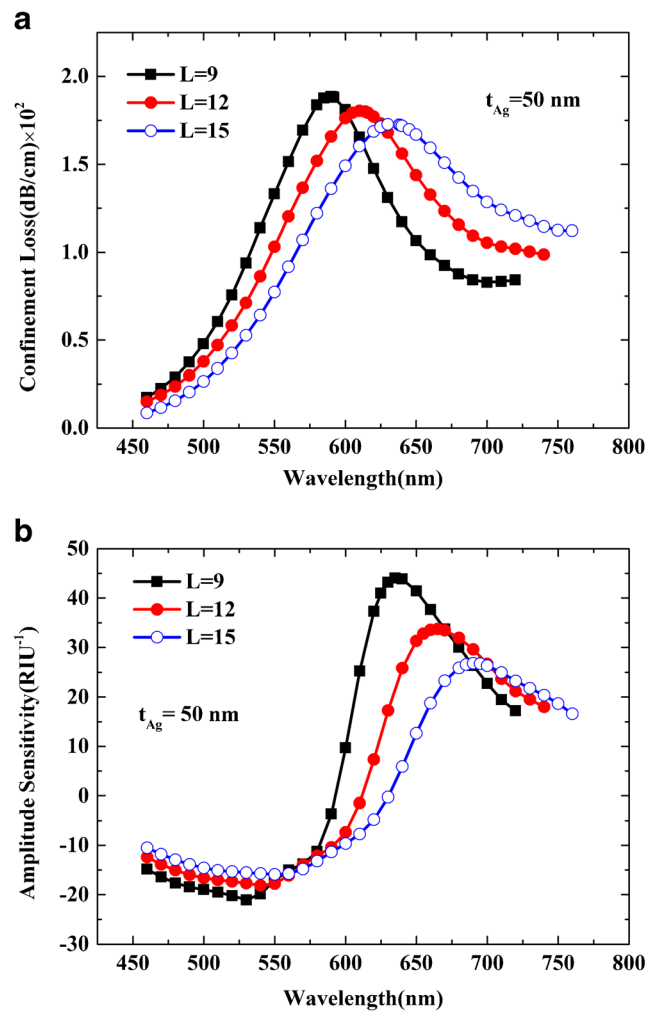


Fig. 9 **a** Loss spectra of the designed sensor when the number of graphene layer $L = 9, 12, 15$ with $n_a = 1.33$, $d_c/\Lambda = 0.5$, $d_2/\Lambda = 0.8$, and $t_{Ag} = 50$ nm. **b** Amplitude sensitivities of the designed sensor when the number of graphene layer $L = 9, 12, 15$ with $n_a = 1.33$, $d_c/\Lambda = 0.5$, $d_2/\Lambda = 0.8$, and $t_{Ag} = 50$ nm

Conclusion

A graphene-based PCF-SPR sensor has been analyzed through FEM by utilizing the COMSOL Multiphysics software in this paper. Wavelength and amplitude interrogations are used to evaluate the sensor’s performance, and the numerical results show that an optimal value of central hole size is existed making the designed sensor most sensitive. The asymmetrical structure only affects the resonance intensity of the sensor, and a trade among confinement loss, wavelength, and amplitude sensitivities is reached when the Ag layer varies. Moreover, a thinner graphene layer can get a sharper resonance peak and a higher sensitivity. The wavelength sensitivity we obtained is as high as 2520 nm/RIU with the resolution of 3.97×10^{-5} RIU, which can provide a reference for developing a high-sensitivity, real-time, fast-response, and distributed SPR sensor.

Acknowledgments This work was supported by the National Basic Research Program of China (973 Program) (grant number: 2010CB327801)

References

- Gupta BD, Verma RK (2009) Surface plasmon resonance-based fiber optic sensors: principle, probe designs, and some applications. *J Sens* 2009:1–12
- Liedberg B, Nylander C, Lunstrom I (1983) Surface plasmon resonance for gas detection and biosensing. *Sensors Actuators* 4(83): 299–304
- Lam WW, Chu LH, Wong CL, Zhang YT (2005) A surface plasmon resonance system for the measurement of glucose in aqueous solution. *Sensors Actuators B* 105:138–143
- Ekgasit S, Tangcharoenbumrungsuk A, Yu F, Baba A, Knoll W (2005) Resonance shifts in SPR curves of nonabsorbing, weakly absorbing, and strongly absorbing dielectrics. *Sensors Actuators B* 105(2):532–541
- Verma A, Prakash A, Tripathi R (2015) Sensitivity enhancement of surface plasmon resonance biosensor using graphene and air gap. *Opt Commun* 357:106–112
- Fu HY, Zhang SW, Chen H, Weng J (2015) Graphene enhances the sensitivity of fiber-optic surface plasmon resonance biosensor. *IEEE Sens J* 15(10):5478–5482
- Rezaei N, Yahaghi A (2014) A high sensitivity surface Plasmon resonance D-shaped fiber sensor based on a waveguide-coupled bimetallic structure: modeling and optimization. *IEEE Sensors J* 14(10):3611–3615
- Kanso M, Cuenot S, Louarn G (2007) Roughness effect on the SPR measurement for an optical fiber configuration: experimental and numerical approaches. *J Opt A Pure Appl Opt* 9(7):586–592
- Moayyed H, Leite IT, Coelho L, Santos JL, Viegas D (2014) Analysis of phase interrogated SPR fiber optic sensors with bimetallic layers. *IEEE Sensors J* 14(10):3662–3668
- Yang XC, Lu Y, Wang MT, Yao JQ (2016) SPR sensor based on exposed-core grapefruit fiber with bimetallic structure. *IEEE Photon Technol Lett* 28(6):649–652
- Wu L, Chu HS, Koh WS, Li EP (2010) Highly sensitive graphene biosensors based on SPR. *Opt Express* 18(14):14395–14400
- Nair RR, Blake P, Grigorenko AN, Novoselov KS, Booth TJ, Stauber T, Peres NMR, Geim AK (2008) Fine structure constant defines visual transparency of graphene. *Science* 320(5881):1308
- Wu ZQ, Chen XD, Zhu SB, Zhou ZW, Yao Y, Quan W, Liu B (2013) *IEEE Sensors J* 13(2):777–782
- Barnes WL, Dereux A, Ebbesen TW (2003) Surface plasmon sub-wavelength optics. *Nature* 424(6950):824–830
- Ortigosa-Blanch A, Knight JC, Wadsworth WJ, Arriaga J, Mangan BJ, Birks TA, Russell PSJ (2000) Highly birefringent photonic crystal fibers. *Opt Lett* 25(18):1325–1327
- Zhao CL, Yang XF, Lu C, Jin W, Demokan MS (2004) Temperature-insensitive interferometer using a highly birefringent photonic crystal fiber loop mirror. *IEEE Photon Technol Lett* 16(11):2535–2537
- Xue JR, Li SG, Xiao YZ, Qin W, Xin XJ, Zhu XP (2013) Polarization filter characters of the gold-coated and the liquid filled photonic crystal fiber based on surface plasmon resonance. *Opt Express* 21(11):13733–13740
- Li H, Li SG, Chen HL, Li JS, An GW, Zi JC (2015) A polarization filter based on photonic crystal fiber with asymmetry around gold-coated holes. *Plasmonics* 11(1):103–108
- Dash JN, Jha R (2015) On the performance of graphene-based D-shaped photonic crystal fibre biosensor using surface plasmon resonance. *Plasmonics* 10(5):1123–1131
- Yu X, Zhang Y, Pan SS, Shum P, Yan M, Leviatan Y, Li C (2010) A selectively coated photonic crystal fiber based surface plasmon resonance sensor. *J Opt* 12(1):015005
- Peng Y, Hou J, Huang ZH, Lu QS (2012) Temperature sensor based on surface plasmon resonance within selectively coated photonic crystal fiber. *Appl Opt* 51(26):6361–6367
- Choi SH, Kim YL, Byun KM (2011) Graphene-on-silver substrates for sensitive surface plasmon resonance imaging biosensors. *Opt Express* 19(2):458–466
- Dash JN, Jha R (2014) Graphene-based birefringent photonic crystal fiber sensor using surface plasmon resonance. *IEEE Photon Technol Lett* 26(11):1092–1095
- Sazio PJA, Adrian AC, Finlayson CE, Hayes JR et al (2006) Microstructured optical fibers as high-pressure microfluidic reactors. *Science* 311(5767):1583–1586
- Harrington JA (2000) A review of IR transmitting, hollow waveguides. *Fiber Integr Opt* 19(19):211–227
- Salihoglu O, Balci S, Kocabas C (2012) Plasmon-polaritons on graphene-metal surface and their use in biosensors. *Appl Phys Lett* 100:1–5
- Liang X, Fu Z, Chou SY (2007) Graphene transistors fabricated via transfer-printing in device active-areas on large wafer. *Nano Lett* 7(12):3840–3844
- Zhang X, Wang R, Cox FM, Kuhlmeier BT, Large MCJ (2007) Selective coating of holes in microstructured optical fiber and its application to in-fiber absorptive polarizers. *Opt Express* 15(24): 16270–16278
- Peng Y, Hou J, Zhang Y, Huang ZH, Xiao R, Lu QS (2013) Temperature sensing using the bandgap-like effect in a selectively liquid-filled photonic crystal fiber. *Opt Lett* 38(3):263–265
- Akowuah EK, Gorman T, Ademgil H, Haxha S, Robinson GK, Oliver JV (2012) Numerical analysis of a photonic crystal fiber for biosensing applications. *IEEE J Quantum Electron* 48(11): 1403–1410
- Palik ED (ed) (1985) *Handbook of optical constants of solids*. Academic, San Diego
- Luan NN, Wang R, Lv WH, Yao JQ (2015) Surface plasmon resonance sensor based on D-shaped microstructured optical fiber with hollow core. *Opt Express* 23(7):8576–8582